

# Nitrogen-Doped and CdSe Quantum-Dot-Sensitized Nanocrystalline TiO<sub>2</sub> Films for Solar Energy Conversion Applications

Tzarara López-Luke,<sup>†,‡</sup> Abraham Wolcott,<sup>†</sup> Li-ping Xu,<sup>†</sup> Shaowei Chen,<sup>†</sup> Zhenhai Wen,<sup>‡</sup> Jinghong Li,<sup>‡</sup> Elder De La Rosa,<sup>§</sup> and Jin Z. Zhang<sup>\*,†</sup>

Department of Chemistry and Biochemistry, University of California, Santa Cruz, California 95064, Instituto de Investigaciones Metalúrgicas, Universidad Michoacana de San Nicolás de Hidalgo, Ciudad Universitaria, Morelia Michoacán, 58060, México, Department of Chemistry, Tsinghua University, Beijing, 100084, China, and Centro de Investigaciones en Óptica, A.P. 1-948, Leon Gto. 37160, México

Received: September 12, 2007; In Final Form: November 2, 2007

Nitrogen-doped titanium dioxide (TiO<sub>2</sub>/N) nanoparticle thin films have been produced by a sol–gel method with hexamethylenetetramine (HMT) as the dopant source. The synthesized TiO<sub>2</sub>/N thin films have been sensitized with CdSe quantum dots (QDs) via a linking molecule, thioglycolic acid (TGA). Optical, morphological, structural, and photocurrent properties of the thin films with and without QD sensitization have been characterized by AFM, TEM, XPS, Raman spectroscopy, UV–visible spectroscopy, and photoelectrochemistry techniques. AFM measurements reveals that films with thicknesses of 150 and 1100 nm can be readily prepared, with an average TiO<sub>2</sub> particle size of 100 nm. TEM shows a uniform size distribution of CdSe QDs utilized in sensitizing the TiO<sub>2</sub>/N films. Doping of the TiO<sub>2</sub> crystal lattice by HMT was confirmed to be 0.6–0.8% by XPS. Differences in crystal phase caused by the precursors HMT, nitric acid, and poly(ethylene glycol) (PEG) are elucidated using XRD and Raman spectroscopy. The resultant crystal phase of TiO<sub>2</sub>/N varies but is a mixture of anatase, brookite, and rutile phases. UV–visible absorption spectra show that N doping of TiO<sub>2</sub> causes a red-shifted absorption into the visible region, with an onset around 600 nm. Nitrogen doping is also responsible for the enhanced photocurrent response of the TiO<sub>2</sub>/N nanoparticle films in the visible region relative to undoped TiO<sub>2</sub> films. In addition, CdSe QDs linked to TiO<sub>2</sub>/N nanoparticles using TGA were found to significantly increase the photocurrent and power conversion of the films compared to standard TiO<sub>2</sub>/N films without QD sensitization. The incident photon-to-current conversion efficiency (IPCE) is 6% at 400 nm for TiO<sub>2</sub>/N–TGA–CdSe solid-state solar cells and 95% for TiO<sub>2</sub>/N–TGA–CdSe films near 300 nm in a Na<sub>2</sub>S electrolyte, which is much higher than that of undoped TiO<sub>2</sub> with QD sensitization or TiO<sub>2</sub>/N without QD sensitization. The power conversion efficiency ( $\eta$ ) was found to be 0.84% with a fill factor (FF%) of 27.7% with 1100 nm thick TiO<sub>2</sub>/N–TGA–CdSe thin films. The results show that combining nitrogen doping with the QD sensitization of TiO<sub>2</sub> thin films is an effective and promising way to enhance the photoresponse in the near-UV and visible region, which is important for potential photovoltaic (PV) and photoelectrochemical applications.

## 1. Introduction

In recent years, there is an increasing interest to find sustainable alternative energy (SAE) sources due to the heightening cost of fossil fuels and the detrimental effects of global climate change. Photovoltaic (PV) cells have received significant attention due to the limitless influx of photons from the sun. Recent market energy analysis is predicting energy parity between conventional energy production and PV costs in cents per kilowatt hour (cents/kW h) in only 5–8 years.<sup>1</sup> Silicon solar cells have attained a solar conversion efficiency of 20%; however, the manufacturing process is very expensive and involves the use of toxic chemicals inherent in the semiconductor industry.

To date, there have been reports of two types of solar cells based on nanostructured semiconductor materials, the Grätzel

solar cell, based on dye-sensitized nanoporous semiconductor thin films,<sup>2</sup> and the quantum dot solar cell, based on composite films of semiconductor nanoparticles (CdSe) and conjugated polymers studied by Greenham et al.<sup>3</sup> Grätzel's initial report in 1991 presented a nanocrystalline dye-sensitized solar cell converting light to electrical energy with an efficiency of 7%. The dye-sensitized solar cell (DSSC) consists of TiO<sub>2</sub> nanoparticles acting as a highly porous, wide band gap semiconductor, electron acceptor layer. In the DSSC, visible-light-absorbing dye molecules adsorbed onto the TiO<sub>2</sub> surface act as the sensitizer to harvest more of the solar flux. Under irradiation, the photoexcited dye molecules inject electrons into the TiO<sub>2</sub> layer that are transported through the porous TiO<sub>2</sub> layer and collected by a conductive fluorine-doped SnO<sub>2</sub> layer on the glass surface. The oxidized dye is regenerated by a liquid electrolyte, with the highest reported efficiency of about 10%. Greenham investigated the processes of charge separation and transport in the interface between a conjugated polymer and semiconductor nanocrystal as a hybrid organic–inorganic system. A quantum efficiency of up to 12% has been reported with a high

\* To whom correspondence should be addressed. E-mail: zhang@chemistry.ucsc.edu. Phone: 831-459-3776.

<sup>†</sup> University of California.

<sup>‡</sup> Universidad Michoacana de San Nicolás de Hidalgo.

<sup>§</sup> Tsinghua University.

<sup>§</sup> Centro de Investigaciones en Óptica.

concentration of nanocrystals, where both nanocrystals and polymers provide continuous pathways to the electrodes.<sup>3</sup> The absorption, charge separation, and transport properties of the composites were found to be a function of the size, material, and the surface ligands of the nanocrystals utilized.

TiO<sub>2</sub> and ZnO nanoparticles represent good examples of nanocrystalline materials used for potentially low-cost PV devices for energy conversion as an alternative to silicon solar cell technology<sup>4–9</sup> and for photocatalysis.<sup>10,11</sup> Titanium dioxide (TiO<sub>2</sub>), or titania, exists in three crystalline phases, anatase, rutile, and brookite. Anatase and rutile have found uses mainly in PV cells, photoelectrochemical cells (PEC), and photocatalysis applications.<sup>12–15</sup> On the contrary, the brookite phase has not received similar attention, perhaps because it is the most difficult to prepare in the form of a thin film.<sup>16</sup> Titania has a wide band gap (3.2 eV) and absorbs only 5% of the solar spectrum, resulting in poor conversion efficiency in solar cell applications. Nonmetal-doped TiO<sub>2</sub> nanoparticles and nanotubes have been shown to produce electronic states in the TiO<sub>2</sub> band gap, thereby extending photoresponse to the visible region and improving photoactivity.<sup>17–19</sup> Recent studies of TiO<sub>2</sub>/N and ZnO/N have found success in narrowing the band gap and increasing light harvesting efficiency with nitrogen doping,<sup>20–22</sup> and further investigations have been focusing on the resulting photoelectrochemical properties and photocatalytic activity for SAE production. Several different synthesis protocols have been developed to produce TiO<sub>2</sub>/N. The usual doping process involves using ammonia as a nitrogen source by sol–gel, thermal, or hydrothermal chemical methods.<sup>23,24</sup>

An alternative method to obtain TiO<sub>2</sub>/N involves using HMT by chemical and mechanochemical processes. The resulting effect on crystalline phase composition showed increased photocatalytic activity and photovoltaic properties, with specific morphologies produced.<sup>25,26</sup> Nitrogen doping within TiO<sub>2</sub> can be interstitial or substitutional, with the latter being more effective, resulting in mixing of N 2p states with O 2p states and contributing to the band gap narrowing.<sup>27,28</sup> Different techniques have been used to study N-doped TiO<sub>2</sub> crystallographically, including XPS, EPR, Raman spectroscopy, XRD, and absorption spectroscopy.<sup>29–31</sup> Theoretical studies have supported the visible absorption and the resulting yellowish color of TiO<sub>2</sub>/N thin films and powders.<sup>32,33</sup>

Alternative techniques to increase the photoresponse besides doping include the utilization of tunable narrow band gap semiconductor nanoparticles or quantum dots (QDs) such as CdS, CdSe, and CdTe to sensitize wide band gap semiconductors such as the metal oxides, for example, TiO<sub>2</sub> and ZnO.<sup>34–37</sup> QDs with their large extinction coefficient strongly absorb visible light, inject electrons into the conduction band of metal oxides, and thereby, contribute to increased solar energy conversion. Attachment of CdSe QDs to nanocrystalline TiO<sub>2</sub> has been shown to be successful with an immersion method using a bimolecular linker.<sup>38</sup> Sonochemical, photodeposition, and chemical bath deposition of CdSe on TiO<sub>2</sub> nanoparticles and nanotubes has also been studied for photocatalysis applications.<sup>39–41</sup> However, the use of QDs to improve TiO<sub>2</sub>-based solar cell efficiency is still an area of active exploration.

In this work, we demonstrate a relatively simple approach to dope TiO<sub>2</sub> nanoparticles with nitrogen and also efficiently sensitize the doped nanoparticles with CdSe QDs. The nanoparticle films have been characterized in terms of their structural, optical, and morphological properties using a combination of experimental techniques. The results show substantially enhanced photoresponse and improved conversion efficiency of

the TiO<sub>2</sub> nanoparticle films when nitrogen doping and QD sensitization are used in unison. Possible explanations are provided in terms of the morphological and optical properties of the films. This method based on combined doping and QD sensitization is promising for solid-state PV cells and photoelectrochemical applications.

## 2. Experimental Section

**2.1. Sample Preparation. Materials.** Titanium(IV) isopropoxide (#377996, 99%), technical-grade trioctylphosphine (TOP-#117854, 90%), trioctylphosphine oxide (TOPO-#223301, 99%), potassium chloride (KCl-#204099, 99%), poly(ethylene glycol) (PEG-#25322–68-3, average  $M_n$  of ca. 10000 g/mol), and sodium sulfide (Na<sub>2</sub>S-#407410, 99%) were obtained from Sigma-Aldrich (Milwaukee, WI). Cadmium oxide (CdO-#223791000, 99%) and selenium powder (Se 200 mesh-#198070500, 99%) were obtained from Acros Organics (Morris Plains, NJ). 1-Tetradecylphosphonic acid (TDPA-#4671–75-4, 99%) was obtained from PCI synthesis (Newburyport, MA). Nitric acid (2.0 N-#LC178502) was purchased from Lab. Chem Inc. (Pittsburgh, PA). Thioglycolic acid (TGA-#103036, 98%) was obtained from MP Biomedicals Inc. (Solon, OH). F/SnO<sub>2</sub> conductive glass (Tec glass 30 Ohms) was obtained from Hartford glass (Hartford City, IN), and the Ag/AgCl reference electrodes were from CH Instruments Inc. (Austin, TX).

**TiO<sub>2</sub> Film Preparation.** Four kinds of TiO<sub>2</sub> films (TiO<sub>2</sub>-1, TiO<sub>2</sub>-2, TiO<sub>2</sub>-3, and TiO<sub>2</sub>-4) were made by a sol–gel method. All TiO<sub>2</sub> films were made using 375  $\mu$ L of titanium isopropoxide as a precursor, which was stored in a nitrogen-filled glovebox. For TiO<sub>2</sub>-1, TiO<sub>2</sub>-2, TiO<sub>2</sub>-3, and TiO<sub>2</sub>-4, titanium isopropoxide was injected into 250  $\mu$ L of Milli-Q water and 5 mL of ethanol within the glovebox. TiO<sub>2</sub>-1 solutions did not contain nitric acid, while TiO<sub>2</sub>-2 solutions contained a dropwise addition of nitric acid until the solution reached a pH  $\sim$  1.23. TiO<sub>2</sub>-3 solutions are similar to TiO<sub>2</sub>-2, but 0.05 g of HMT was added under vigorous stirring. Solution TiO<sub>2</sub>-4 is similar to TiO<sub>2</sub>-3, with an addition of 0.90 g of poly(ethylene glycol) (PEG-10,000 g/mol) under vigorous stirring, all within an O<sub>2</sub>-free environment. As a point of clarification, acidification (TiO<sub>2</sub>-2, TiO<sub>2</sub>-3, and TiO<sub>2</sub>-4) was performed outside of the glovebox prior to titanium isopropoxide addition within the glovebox. The sol was then stirred for 3 days within the glovebox at ambient temperatures ( $\sim$ 25  $^{\circ}$ C). All TiO<sub>2</sub> films were made by spin coating at 2000 rpm for 60 s onto FTO (SnO<sub>2</sub>/F) conducting substrates in ambient conditions. The thickness was estimated with the mass, area, and density of the TiO<sub>2</sub> films and was confirmed with AFM measurements ( $\sim$ 150 and  $\sim$ 1100 nm thick). The films were annealed at 550  $^{\circ}$ C for 1.5 h with a Leister heat gun in open air conditions. For thin TiO<sub>2</sub>-1, TiO<sub>2</sub>-2, TiO<sub>2</sub>-3, and TiO<sub>2</sub>-4 films, 50, 200, 100, and 50  $\mu$ L of the sol solution was used, respectively. For thick TiO<sub>2</sub>-1, TiO<sub>2</sub>-2, TiO<sub>2</sub>-3, and TiO<sub>2</sub>-4 films, 400, 2000, 700, and 250  $\mu$ L, respectively, of the sol solution was used. The sol solution was put on the conductive glass with 2.2 cm<sup>2</sup> areas. It was necessary to apply different volumes in order to obtain approximately the same film thickness because of the different viscosities of the various solutions.

**CdSe QD Synthesis.** High-quality CdSe QDs were synthesized based upon the protocol of Peng et al.,<sup>42</sup> wherein CdO is utilized as the Cd precursor and TDPA and TOPO are the ligands and coordinating solvents, respectively. The resulting CdSe nanocrystals were in the strong confinement size regime and were synthesized in normal air-free reaction conditions. The synthesis of the CdSe nanoparticle follows the procedure reported by Robel et al., wherein 0.05 g ( $\sim$ 0.39 mmol) of CdO, 0.3 g ( $\sim$ 1.1

mmol) of TDPA, and 4 g of TOPO were heated to 110 °C and degassed under vacuum and then heated to 300 °C under a nitrogen flow (Schlenk line).<sup>38</sup> A SeTOP (0.7% by weight) solution was obtained by adding 0.026 g of Se powder with 4.25 mL of TOP inside of a glovebox and stirring for 1 h to ensure complete dissolution of the Se powder. After reaching 300 °C, the Cd–TDPA–TOPO solution was cooled to 270 °C prior to the injection of SeTOP. Under a nitrogen flow, 3 mL of SeTOP was injected, which resulted in the lowering of the temperature to 260 °C. The temperature was then increased to 280 °C to facilitate particle growth, and aliquots were removed and probed to track nanocrystallite growth via UV–vis absorption spectroscopy and photoluminescence (PL) spectroscopy. The CdSe solution was cooled and was removed from the reaction flask at around 80 °C and dissolved into ~10 mL of toluene. The QDs in toluene were then cleaned twice through a precipitation and decantation regime using methanol and centrifugation at 3000 rpm, and the QDs were ultimately redissolved in toluene prior to their use as a sensitizer.

**CdSe QD Linkage to TiO<sub>2</sub>.** CdSe QDs were linked to nanocrystalline TiO<sub>2</sub> and TiO<sub>2</sub>/N thin films using TGA as a molecular linker. TiO<sub>2</sub> has a strong affinity for the carboxylate group of the linker molecules, while the sulfur atom of TGA binds strongly to CdSe nanoparticles through surface Cd<sup>2+</sup> cations. The films were dried with a heat gun at 100 °C for 4 h to remove H<sub>2</sub>O from the surface due to ambient humidity adsorption. They were later immersed in undiluted neat TGA for 12 h in a nitrogen environment in a glovebox. The films were then immersed in toluene, removing the excess TGA, and in turn immersed in a CdSe solution for 12 h inside of the glovebox. Four films of 2.2 cm<sup>2</sup> were immersed in 5 mL of CdSe QDs suspended in toluene, as described earlier. The TiO<sub>2</sub>/N–TGA–CdSe films were stored in a nitrogen-filled glovebox and not exposed to light prior to PEC characterization. The solid-state TiO<sub>2</sub>/N–TGA–CdSe cell after PEC measurements remained stable for months. The TiO<sub>2</sub>/N–TGA–CdSe cell in the electrolyte is very stable; however, when it is removed from the Na<sub>2</sub>S electrolyte and are in ambient conditions, the thin films' properties deteriorate after experimentation. Long-term stability needs to be further studied in future research.

**2.2. Structural and Morphological Characterization.** X-ray photoelectron spectroscopy (XPS) studies of the films were carried out on an X-ray photoelectron spectrometer (XPS, PHI Quantera SXM) using a non-monochromatized Al K $\alpha$  X-ray source (1486.6 eV). The energy resolution of the spectrometer was set at 0.5 eV. The binding energy was calibrated using a C 1s (284.6 eV) spectrum of a hydrocarbon that remained in the XPS analysis chamber as a calibration tool. Crystalline phase identification was performed via X-ray diffraction (XRD) in conjunction with Raman spectroscopy. XRD analysis was conducted on a MINIFLEX diffractometer operating at 30 kV/15 mA using Cu–K $\alpha$  radiation and a scanning speed of 1°/2 $\theta$ /min.

Raman spectroscopy of the films was performed using a Renishaw micro-Raman setup with a (5/10/20/50)× objective lens and a 633 nm wavelength laser (Research Electro-Optics, Inc., Boulder, CO). Renishaw's WiRE (Windows-based Raman environment) was used for collection and data analysis of 1–5 scans ranging in accumulations of 1–10 s.

AFM images of the films without and with QDs were acquired under ambient conditions with a PicoLE SPM instrument (Molecular Imaging) in tapping mode. The tapping mode cantilevers exhibit resonant frequencies between 60 and 90 kHz (typical 75 kHz), force constants of 2.5–5.5 N/m, and tip apex

radii of ~10 nm. The resulting images were flattened and plane-fitted using software from Molecular Imaging. Silica-etched tips were purchased from MikroMasch (Watsonville, OR).

A JEOL model JEM-1200EX microscope was used for the low-resolution transmission electron microscope (TEM) studies of the CdSe QDs. The TEM was equipped with a Gatan Model 792 Bioscan digital camera running on a Windows 2000 computer with the Gatan Digital micrograph as the analyzing software.

**2.3. Optical and Electrochemical Characterization.** UV–vis absorption spectroscopy was conducted on a Hewlett-Packard 8452A diode array spectrophotometer. UV–vis absorption spectra were measured first by placing a blank FTO glass substrate in the light path, subtracting the absorption pattern, and then performing the UV–vis absorption measurement on the collection of TiO<sub>2</sub> thin films.

Photoluminescence (PL) spectroscopy was gathered on a Perkin-Elmer LS 50B with an excitation wavelength of 390 nm and a 1% attenuator. QDs in toluene were placed in an open-sided 1 cm path length quartz cuvette for both UV–vis absorption and PL measurements. Thin films were placed in a thin film sample holder from Perkin-Elmer (#52123130) for PL spectra.

Photoelectrochemical studies (linear sweep voltammetry and incident photon-to-current conversion efficiency (IPCE)) in the solid state and in an electrolyte were carried out with a CHI440 electrochemical workstation (Austin, TX). Linear sweep voltammetry was used to obtain the I–V profiles. Actively investigated thin films were the TiO<sub>2</sub>, TiO<sub>2</sub>/N, and TiO<sub>2</sub>/N–CdSe thin films described earlier. A Ag/AgCl and Pt wire coil were used as the reference and counter electrodes, respectively. Before each measurement, the Na<sub>2</sub>S electrolyte solution was deaerated by bubbling ultrahigh-purity N<sub>2</sub> for 20 min through the electrolyte solution, and a nitrogen flow was also subsequently blown over the surface during data gathering. For I–V measurements, a halogen lamp was utilized (75 W), and for IPCE measurements, a 1000W Xe lamp (Oriel Research arc lamp assembly #69924 and power supply #69920) coupled to an infrared (IR) water-filled filter (Oriel # 6127) was used and then aligned into a monochromator (Oriel Cornerstone 130 1/8m) for spectral resolution from 300 to 800 nm. An aqueous Na<sub>2</sub>S solution served as the redox couple to maintain the stability of the QDs, as discussed elsewhere.<sup>43,44</sup> A maximum photocurrent was produced with 1 M Na<sub>2</sub>S using 6.5 mL of Milli-Q water (18 M $\Omega$ ). Diminished molarities of Na<sub>2</sub>S were found to decrease the overall photocurrent performance. IPCE measurements were also conducted for solid-state TiO<sub>2</sub>/N–TGA–CdSe solar cells. A schematic of the photoelectrochemical setup is shown in Figure 1a,b.

### 3. Results

The amount of nitrogen in N-doped TiO<sub>2</sub> nanoparticle films was identified by the XPS technique. Figure 2 shows the XPS spectra for the TiO<sub>2</sub>-3 film. Figure 2a shows the Ti 2p, O 1s, C 1s, N 1s, and Sn binding energies from 0 to 1000 eV (Sn is identified from the conductive film). Figure 2b shows only the nitrogen binding energy from 396 to 408 eV, showing two peaks at 400 and above 401.2 eV. To compare the effect of HMT and PEG, the TiO<sub>2</sub>-3 film has 37.45% of C, 0.60% of N, 50.16% of O, and 11.79% of Ti. The TiO<sub>2</sub>-4 film shows elemental compositions of C and N of 39.93 and 0.80%, respectively, with 48% of O and 11.27% of Ti.

Figure 3 shows the XRD patterns for all of the films prepared for determining the crystal phases of both TiO<sub>2</sub> and TiO<sub>2</sub>/N.

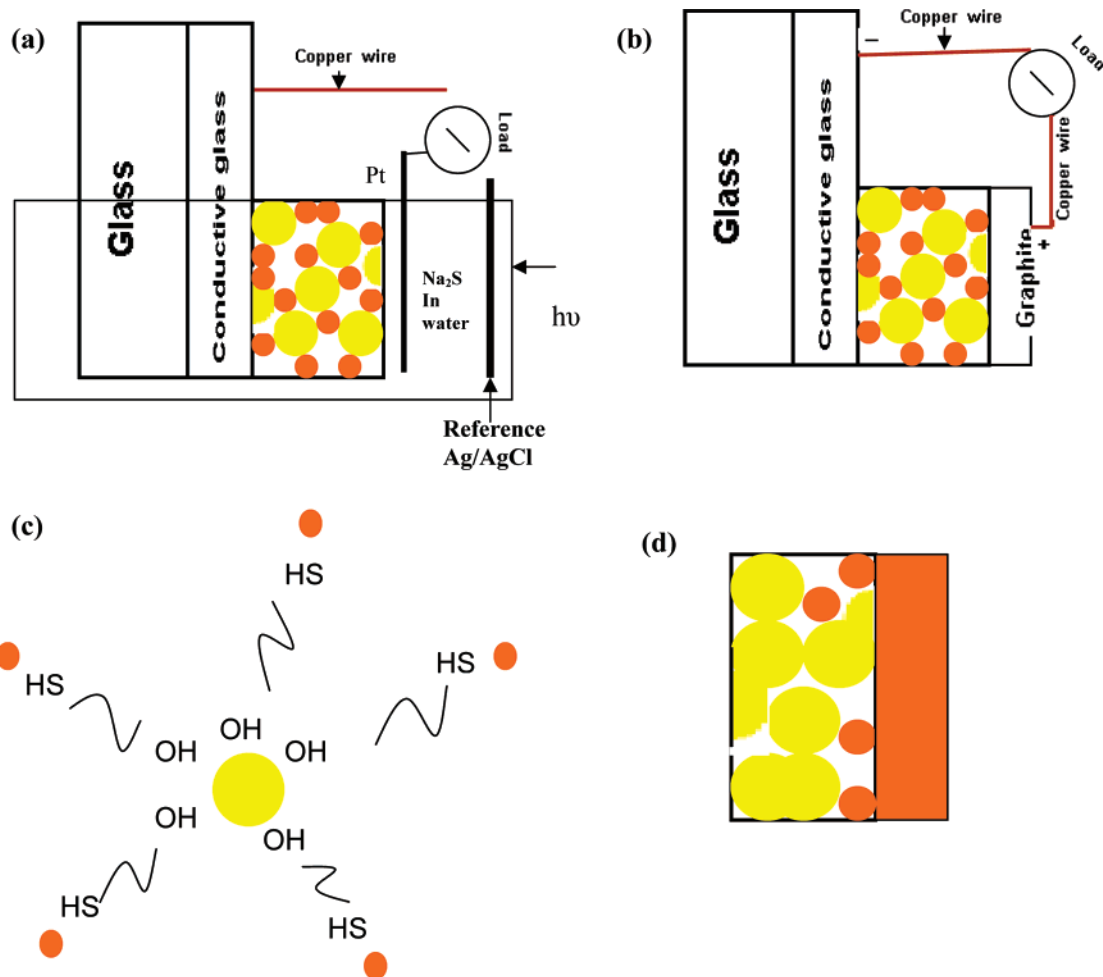


**Figure 1.** Photovoltaic schematic of TiO<sub>2</sub>/N-TGA-CdSe cells in a (a) Na<sub>2</sub>S electrolyte and a (b) solid. (c) Representation of TiO<sub>2</sub>-3 and TiO<sub>2</sub>-4 nanoparticles functionalized with CdSe linked with a bifunctional molecule TGA in a porous film (using HMT and HMT + PEG in the TiO<sub>2</sub> synthesis, respectively). (d) Representation of a TiO<sub>2</sub>-1-TGA-CdSe film (without nitric acid) and a TiO<sub>2</sub>-2-TGA-CdSe film (using nitric acid in the TiO<sub>2</sub> synthesis) with low porosity.

All of the XRD data show the crystal phase of the conductive glass (SnO<sub>2</sub>/F), which is marked as SnF. The TiO<sub>2</sub>-1 film (without nitric acid) XRD pattern is representative of the anatase crystal phase (Figure 3a). For the TiO<sub>2</sub>-2 film (with nitric acid), the brookite and rutile phases appear, with a mix of anatase, brookite, and rutile phases (Figure 3b). With HMT added for the TiO<sub>2</sub>-3 film, a mixture of brookite and rutile phases dominates, with a trace amount of the anatase phase (Figure 3c). With further addition of PEG and HMT, as in the TiO<sub>2</sub>-4 film, the brookite and rutile phases decrease, and the anatase is predominant. Additional evidence for the various crystal phases of the different films comes from their Raman spectra that show anatase as the primary phase for TiO<sub>2</sub>-1 and TiO<sub>2</sub>-4 (Figure 4a and c) and a mix of anatase, brookite, and rutile phases in TiO<sub>2</sub>-2 and TiO<sub>2</sub>-3 films. Representative Raman spectrum of the TiO<sub>2</sub>-3 film is shown in Figure 4b. It can be seen that the characteristic peak for the anatase phase at 144 cm<sup>-1</sup> shifts slightly to 146 cm<sup>-1</sup> with nitrogen doping (TiO<sub>2</sub>-3 and TiO<sub>2</sub>-4 films).

The morphology of the films with and without QDs was studied by AFM in ambient conditions. The average TiO<sub>2</sub> nanocrystal size was found to be around 100 nm in diameter. Films with HMT (TiO<sub>2</sub>-3) or HMT plus PEG (TiO<sub>2</sub>-4) show more porosity than TiO<sub>2</sub>-1 and TiO<sub>2</sub>-2 films. A representative AFM image for the TiO<sub>2</sub>-3 film with about 150 nm thickness is shown in Figure 5a. For thicker films (e.g., 1100 nm), TiO<sub>2</sub> particles were observed to form clusters. All films showed the

presence of CdSe QDs after they were sensitized, as exemplified by the AFM image for the TiO<sub>2</sub>-3-TGA-CdSe film shown in Figure 5b. While it is not easy to determine the exact size of the CdSe QDs based on AFM, the average size of the QDs appear to be on the order of a few nanometers. To better characterize the CdSe QDs, TEM measurements were conducted. Figure 6 shows a representative TEM image of CdSe QDs. The image appears to show reasonably uniform size distributions of the CdSe QDs, with an average diameter of 3.5 nm.

Optical absorption of the different films was characterized by UV-vis spectroscopy, with emphasis on comparing the effect of nitrogen doping through HMT or nitric acid. Figure 7 shows a comparison of the UV-vis absorption spectra of different films. For films without HMT and PEG (TiO<sub>2</sub>-1 and TiO<sub>2</sub>-2), the absorption is primarily around 340 and 400 nm (Figure 7a and b). However, for films with HMT (TiO<sub>2</sub>-3 and TiO<sub>2</sub>-4), the spectra show an obvious red shift of the absorption edge toward the visible region, with peaks around 350, 426, and 542 nm (Figure 7c) or 412 and 532 nm and an absorption onset at 600 nm (Figure 7d). Figure 7e shows the UV-vis absorption spectrum of the TiO<sub>2</sub>-3-CdSe film, with strong absorption around 560 nm due to the CdSe QDs. For comparison, Figure 8a and b shows the absorption and photoluminescence (PL) spectra of CdSe QDs in toluene under ambient conditions. The absorption spectrum shows the expected strong and sharp excitonic peak around 560 nm, while the PL spectrum shows a

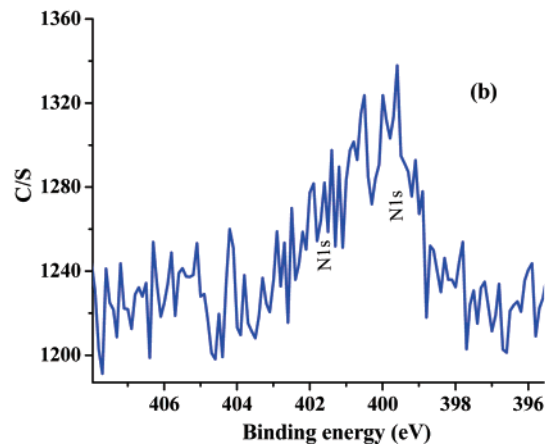
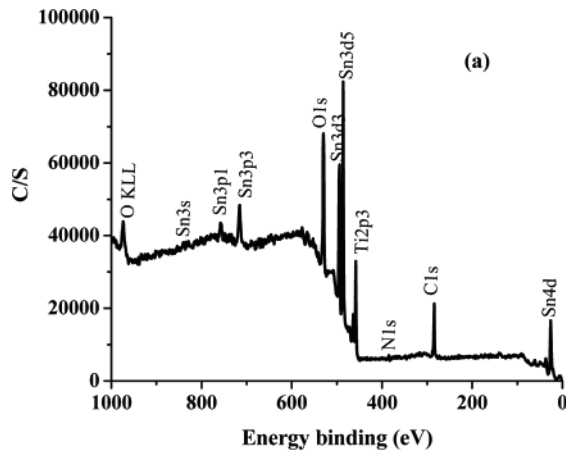


**Figure 2.** (a) XPS spectra of a nitrogen-doped TiO<sub>2</sub>-3 film on a SnO<sub>2</sub>/F substrate showing C, N, Ti, O, and Sn spectra peaks. (b) A detailed N 1s XPS band.

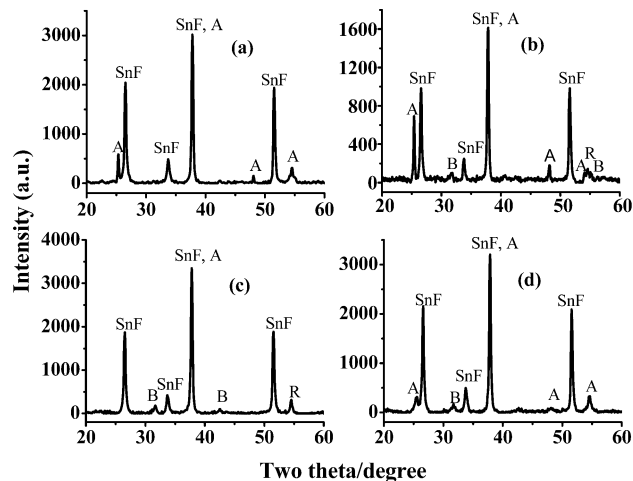


**Figure 3.** XRD patterns of TiO<sub>2</sub> films on the SnO<sub>2</sub>/F substrate prepared by the sol-gel method, using different chemicals in the TiO<sub>2</sub> synthesis, annealed at 550 °C for 1.5 h with a heat gun for (a) a TiO<sub>2</sub>-1 film (without nitric acid), (b) a TiO<sub>2</sub>-2 film (using nitric acid), (c) a TiO<sub>2</sub>-3 film (using nitric acid and HMT), and (d) TiO<sub>2</sub>-4 (using nitric acid, HMT and PEG). The phases found in the films are anatase, rutile, and brookite, marked by A, R, and B, respectively. SnF represents the crystal phase of the conductive glass (SnO<sub>2</sub>/F).

narrow emission band near 580 nm, which is clearly due to band edge emission. Figure 8c shows the PL spectrum of the TiO<sub>2</sub>-3-TGA-CdSe film, with a relatively weak emission peak at 575.5 nm, which is slightly blue-shifted with respect to the PL peak of CdSe QDs in toluene solution.

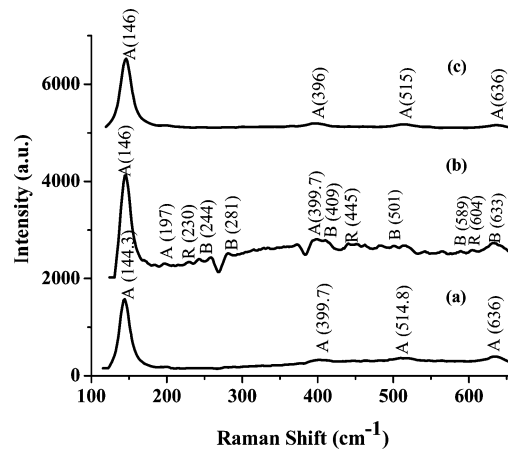


**Figure 4.** TiO<sub>2</sub> film Raman spectra of (a) TiO<sub>2</sub>-1 (without nitric acid, HMT, or PEG), (b) TiO<sub>2</sub>-3 (using nitric acid and HMT in the synthesis), and (c) TiO<sub>2</sub>-4 (using nitric acid, HMT, and PEG in the synthesis).

The current–voltage (*I*–*V*) profiles for solar cells fabricated using films with different thicknesses (150 and 1100 nm) were obtained using a halogen lamp and 1 M Na<sub>2</sub>S. With the cell configuration shown schematically in Figure 1, the *I*–*V* profiles measured are shown in Figure 9. The cell without HMT (TiO<sub>2</sub>-1–CdSe film) presents a low short-circuit current density of  $-169 \mu\text{A}/\text{cm}^2$  with an open-circuit voltage of  $-1.3\text{ V}$  (Figure 9a) within the voltage window of  $-1.4$ – $0.3\text{ V}$ , and the fill factor is 14.8% with a low power conversion efficiency of  $\eta = 0.120\%$ . For the cell based on the TiO<sub>2</sub>-3–TGA–CdSe thin film (150 nm), the *I*–*V* curve in Figure 9b shows a short-circuit current ( $-242 \mu\text{A}/\text{cm}^2$ ) with an open-circuit voltage of  $-1.0\text{ V}$ , a fill factor of 25.4%, and a power efficiency of  $\eta = 0.228\%$ . The cell based on the TiO<sub>2</sub>-3–TGA–CdSe thick film (1100 nm) has the highest short-circuit ( $-683 \mu\text{A}/\text{cm}^2$ ) with an open-circuit voltage of 1.2 V (Figure 9c) and the highest fill factor of 27.7% and a power conversion efficiency of  $\eta = 0.840\%$ . The short-circuit current and open-circuit voltage found in Figure 9 are summarized in Table 1.

The fill factor (FF) and power conversion efficiency ( $\eta\%$ ) were calculated using the short-circuit current and open-circuit voltage<sup>45</sup> and are also given in Table 1

$$\text{FF} = (jV_{\text{max}})/(j_{\text{sc}}V_{\text{oc}}) \quad (1)$$

$$\eta = (jV_{\text{max}})/I_i = \text{FF}(j_{\text{sc}}V_{\text{oc}})/I_i \quad (2)$$

where  $j_{\text{sc}}$  is the short-circuit current density,  $V_{\text{oc}}$  is the open-circuit voltage,  $jV_{\text{max}}$  is the maximum power observed from the current density–voltage curve for each device, and  $I_i$  is the incident light power density ( $27 \text{ mW}/\text{cm}^2$ ). It is clear that thick films ( $\sim 1100\text{ nm}$ ) exhibit a higher FF and  $\eta\%$  than thin films ( $\sim 150\text{ nm}$ ). However, cells with TiO<sub>2</sub>/N nanoparticles sensitized with CdSe QDs exhibit a much higher  $\eta\%$  than films without sensitization.

The incident photon-to-current conversion efficiency (IPCE) was studied for solid cells and in an electrolyte (1M Na<sub>2</sub>S) with different thicknesses. The IPCE at different wavelengths was determined from the short-circuit photocurrent ( $j_{\text{sc}}$ ), where  $V = 0$  at different excitation wavelengths ( $\lambda$ ) using the expression

$$\text{IPCE}\% = [(1240 \times j_{\text{sc}}(\text{A}/\text{cm}^2))/[\lambda(\text{nm}) \times I_i(\text{W}/\text{cm}^2)]] \times 100 \quad (3)$$

where  $I_{\text{inc}}$  is the incident light power. The IPCE results of TiO<sub>2</sub>

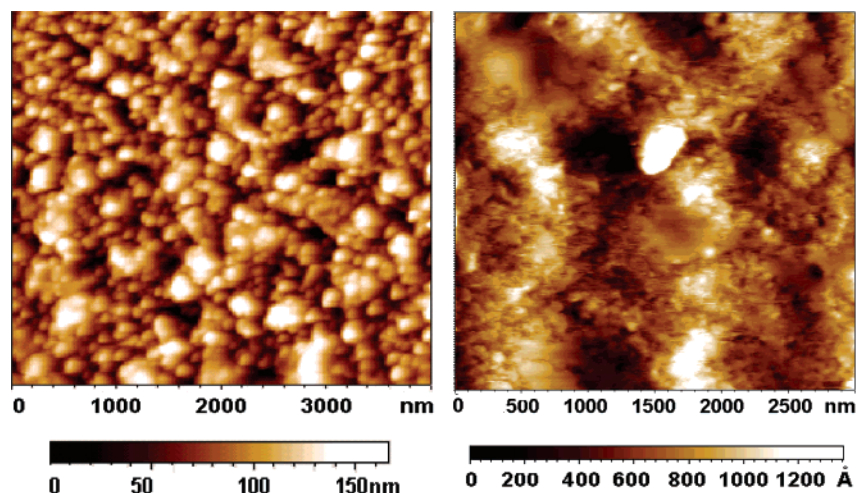


**Figure 5.** AFM images of (left) a nitrogen-doped TiO<sub>2</sub>-3 thin film (175 nm) and (right) N-doped TiO<sub>2</sub>-3 nanoparticles linked to TGA-CdSe nanoparticles (film thickness  $\sim$  1100 nm).

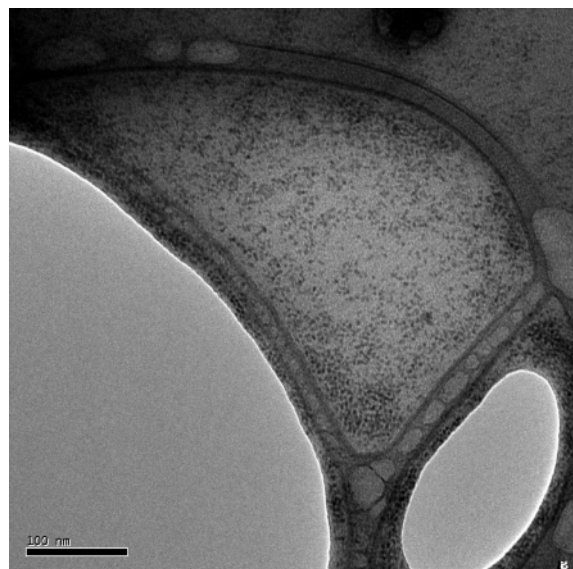


**Figure 6.** Representative TEM image of CdSe quantum dots showing an average particle size around 3.5 nm.

and TiO<sub>2</sub>/N without and with CdSe QDs are shown in Figure 10. It is clear that the photocurrent response is much stronger with the presence of CdSe QD sensitization. The TiO<sub>2</sub>-1-TGA-CdSe film (QD-sensitized but without N doping) shows photocurrent responses at 300, 530, and 620 nm, with the highest response near 300 nm with IPCE = 56%. The TiO<sub>2</sub>-3-TGA-CdSe film (QD-sensitized and N-doped) shows similar response but an overall stronger IPCE with the highest response around 95% at 300 nm. The IPCEs of both films closely match the absorption spectrum of CdSe QDs and TiO<sub>2</sub>/N, as shown in Figure 7e. The IPCE% is 1.06 at 300 nm for TiO<sub>2</sub>/N (magnified 10 $\times$  in Figure 10), showing photocurrent responses at 320, 360, and 420 nm, which are also close to the absorption spectrum as shown in Figure 7c.

In addition, the IPCE% of TiO<sub>2</sub>-3-TGA-CdSe thin film (150 nm) solid cell was studied, and the result is shown in Figure 11. It can be seen that peaks at 480 and 600 nm correspond to absorption of the CdSe QDs (see Figure 11 inset that shows the absorption and emission spectra of the CdSe nanoparticles in toluene). This cell shows an IPCE response around 6% at 400 nm, and the results are summarized in Table 2.

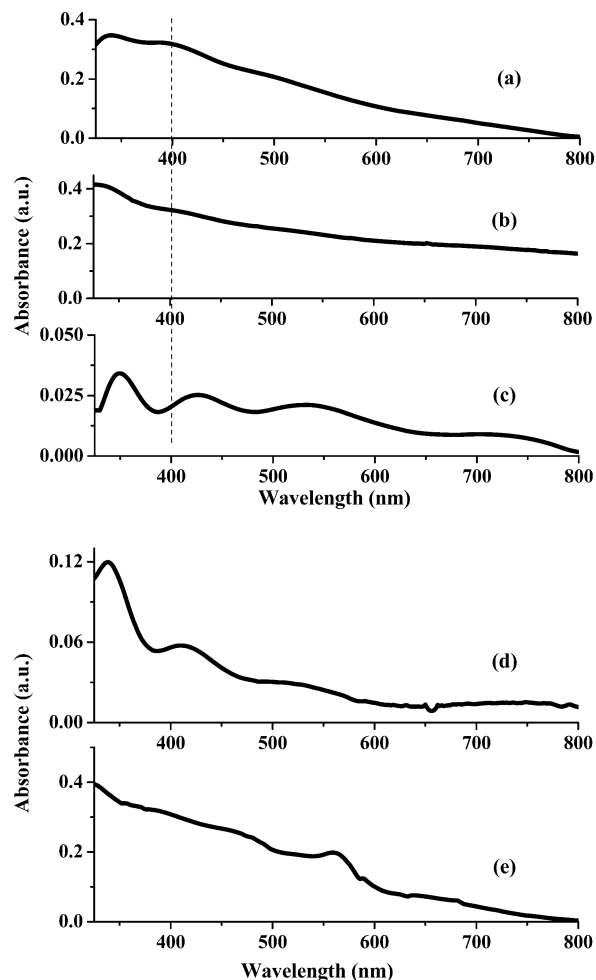


**Figure 7.** UV-vis absorption spectra of the films (a) TiO<sub>2</sub>-1 (without nitric acid), (b) TiO<sub>2</sub>-2 (using nitric acid in the synthesis without HMT), (c) TiO<sub>2</sub>-3 (synthesized with nitric acid and HMT), (d) TiO<sub>2</sub>-4 (synthesized with HMT and PEG), and (e) TiO<sub>2</sub>-3-TGA-CdSe. The blank was the substrate of SnO<sub>2</sub>/F (of the conductive glass).

#### 4. Discussion

**4.1. N Doping of TiO<sub>2</sub> Nanoparticles with HMT.** It is known that HMT hydrolyzes in aqueous solutions to form

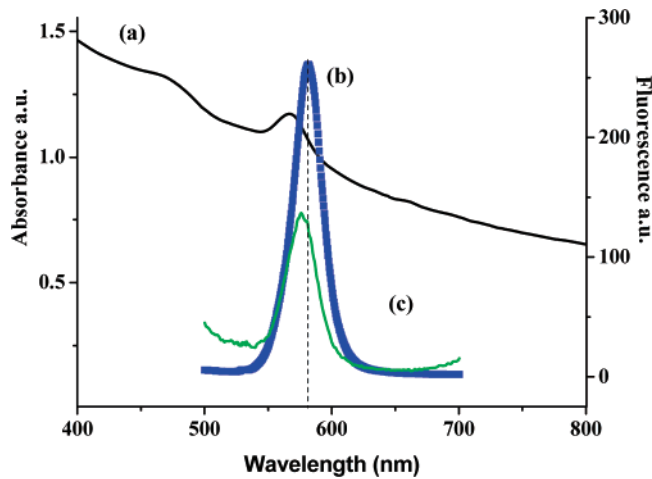


**Figure 8.** UV-vis absorption spectra of (a) CdSe nanoparticles and (b) photoluminescence (PL) spectra of CdSe nanoparticles in toluene excited at 390 nm. (c) Photoluminescence of a TiO<sub>2</sub>-3 film doped with nitrogen and sensitized with CdSe QDs.

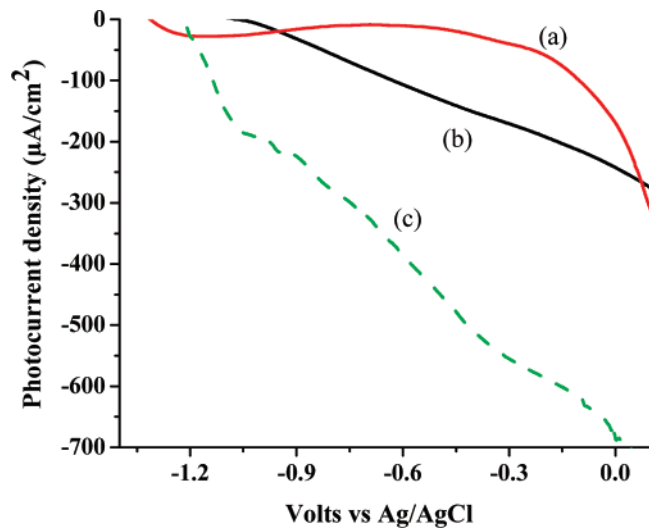
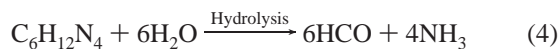


**Figure 9.** *I*-*V* characteristic of (a) a TiO<sub>2</sub>-1-TGA-CdSe thick film, (b) a TiO<sub>2</sub>-3-TGA-CdSe thin film, and (c) a TiO<sub>2</sub>-3-TGA-CdSe thick film using 1 M Na<sub>2</sub>S, excited with a halogen lamp with an incident light intensity of *I*<sub>1</sub> = 27 mW/cm<sup>2</sup>.

ammonia and formaldehyde above 70 °C,<sup>26</sup> as shown in the following equation



Ammonia reacts with Ti(OCH(CH<sub>3</sub>)<sub>2</sub>)<sub>4</sub> (TTIP) to form a

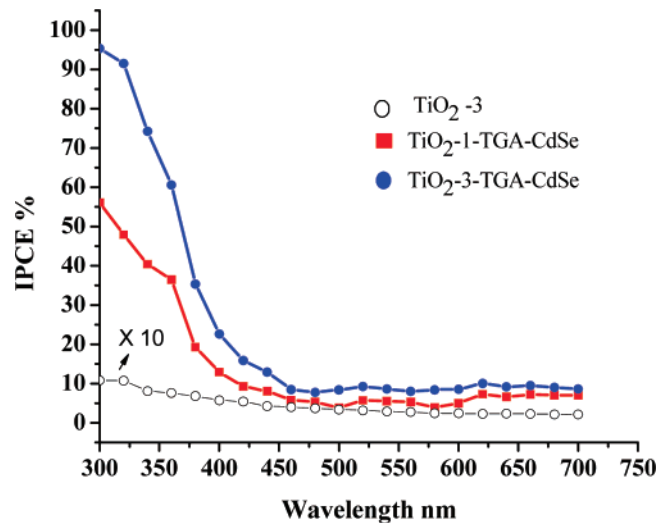
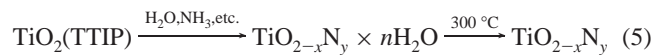


**Figure 10.** IPCE% of the different cells with (○) a TiO<sub>2</sub>-3 film without QD sensitization, (this curve is amplified 10×), (■) a TiO<sub>2</sub>-1-TGA-CdSe film with QD sensitization, and (●) a TiO<sub>2</sub>-3-TGA-CdSe film with QD sensitization.

nitrogen-containing precursor (TiO<sub>2-x</sub>N<sub>y</sub>·nH<sub>2</sub>O). Dehydration of the TiO<sub>2</sub> complex in pure and doped TiO<sub>2</sub> samples is completed at temperatures below 200 °C, and NH<sub>3</sub> molecules remain until the calcination temperature rises to 300 °C. Therefore, crystallization of TiO<sub>2-x</sub>N<sub>y</sub> can be summarized as



A yellowish tint was observed in all films synthesized with HMT or HMT plus PEG, suggesting the presence of a TiO<sub>2</sub>/N sol-gel solution.<sup>32</sup> The XPS spectra for all of the films showed two evident peaks corresponding to Ti 2p and O 1s at 458.5 and 531.5 eV binding energies, accompanied by traces of Sn from a conductive SnO<sub>2</sub>/F film over which the TiO<sub>2</sub> films were formed. Also, traces of carbon at 284 eV were also present due to the intentional hydrocarbon contamination used for calibration. The carbon (C 1s) atom percentage increases from 29% for TiO<sub>2</sub>-1 to 37% and 40% for TiO<sub>2</sub>-3 and TiO<sub>2</sub>-4, respectively. The TiO<sub>2</sub>-4 prepared with both HMT and PEG contains the highest carbon content, which may be attributed to uncombusted material from the precursor solutions, including HMT and PEG. The sample prepared with PEG, TiO<sub>2</sub>-4, contains the highest carbon content. Sample TiO<sub>2</sub>-2 prepared with nitric acid and without HMT in vacuum presents extremely weak nitrogen signals at 401.2 eV. However, TiO<sub>2</sub>-3 and TiO<sub>2</sub>-4 films exhibit N 1s at ~400 and 401.2 eV, which are indicative of nitrogen

**TABLE 1: Summary of the Fill Factor and Power Conversion Efficiency Results From Our Study of a N-TiO<sub>2</sub>-TGA-CdSe-Based Solar Cell in an Electrolyte (Na<sub>2</sub>S); The Power Light is 27 mW/cm<sup>2</sup> (1/4 of AM1.5) Equivalent to Irradiance**

| cell                         | $-I_{sc}$<br>( $\mu\text{A}/\text{cm}^2$ ) | $-V_{oc}$<br>V vs Ag/AgCl | (JV) <sub>max</sub><br>( $\mu\text{A}/\text{cm}^2 \times \text{V}$ ) | fill factor<br>(FF%) | power conversion<br>efficiency<br>( $\eta\%$ ) |
|------------------------------|--|---------------------------|--|----------------------|--|
| Thin Films                   |  |                           |  |                      |  |
| TiO <sub>2</sub> -1          | 19   | 0.5                       | 9.5  | 14.1                 | $4.96 \times 10^{-3}$                          |
| TiO <sub>2</sub> -3          | 19   | 0.7                       | 13.3   | 14.5                 | $7.14 \times 10^{-3}$                          |
| TiO <sub>2</sub> -4          | 19   | 0.74                      | 14.1   | 11.3                 | $5.88 \times 10^{-3}$                          |
| TiO <sub>2</sub> -3-TGA-CdSe | 242  | 1.0                       | 242  | 25.4                 | $2.28 \times 10^{-1}$                          |
| Thick Films                  |  |                           |  |                      |  |
| TiO <sub>2</sub> -1          | 25   | 0.5                       | 12.5   | 24                   | $1.11 \times 10^{-2}$                          |
| TiO <sub>2</sub> -1-TGA-CdSe | 169  | 1.3                       | 219.7  | 14.8                 | $1.20 \times 10^{-1}$                          |
| TiO <sub>2</sub> -2-TGA-CdSe | 400  | 1.2                       | 480  | 41                   | $7.29 \times 10^{-1}$                          |
| TiO <sub>2</sub> -3-TGA-CdSe | 683  | 1.2                       | 819  | 27.7                 | $8.40 \times 10^{-1}$                          |
| TiO <sub>2</sub> -4-TGA-CdSe | 390  | 0.62                      | 241  | 10.37                | $9.25 \times 10^{-2}$                          |

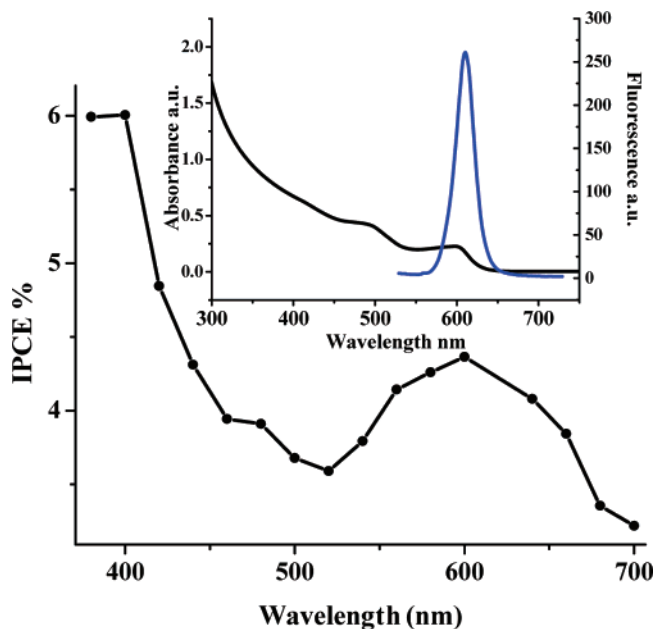


**Figure 11.** IPCE% of the solid-state cell of a TiO<sub>2</sub>-3-TGA-CdSe film in open air conditions. The inset shows UV-vis and PL spectra of CdSe QDs in toluene, with an average size of 4.6 nm, utilized to sensitize the nitrogen-doped TiO<sub>2</sub>-3 film.

**TABLE 2: Summary of IPCE Results from Our Study of Thin and Thick Film-Based Solar Cells in an Electrolyte (Na<sub>2</sub>S) and the Solid State; A Xenon Lamp (1000 W) Was Used, Varying the Wavelength with a Monochromator**

| film type                             | IPCE% (300 nm) |
|---------------------------------------|----------------|
| TiO <sub>2</sub> -1-CdSe thick film   | 56             |
| TiO <sub>2</sub> -2-CdSe thick film   | 65             |
| TiO <sub>2</sub> -3-CdSe thick film   | 95             |
| TiO <sub>2</sub> -4-CdSe thick film   | 53             |
| TiO <sub>2</sub> -4-CdSe thin film    | 2.5            |
| TiO <sub>2</sub> -3 thick film        | 1.06           |
| TiO <sub>2</sub> -3-CdSe thin (solid) | 6 (400 nm)     |

incorporation. We attribute N 1s at 400 eV to N atoms from N-N, N-H, O-N, or N-containing organic compounds absorbed on the surface.<sup>17</sup> It has been reported that N 1s features appearing above 400 eV are due to a Ti-O-N linkage,<sup>20</sup> suggesting that doping within the crystal lattice is, in fact, interstitial in nature.

On the basis of the XRD patterns of different TiO<sub>2</sub> films (Figure 3), nitric acid, HMT, and PEG seem to have a significant effect on the TiO<sub>2</sub> crystalline structure. The phase composition appears to be strongly related to the added quantity of nitric acid and, therefore, to pH. The film prepared without nitric acid shows a pure anatase structure (Figure 3a). A reduction of the pH to 1.23 results in the appearance of rutile and brookite phases mixed with anatase (Figure 3b). However, for the samples prepared with HMT at pH ~ 1.65, the anatase phase decreases (Figure 3c). These results suggest that nitric acid and HMT promote the formation of brookite and rutile phases. The reason for this is not yet clear and needs further study. When added, PEG increases the pH to ~2.06, and the corresponding film shows a presence of the brookite and rutile phases (Figure 3d). Further research is also needed to understand the possible

correlation between the different crystal phases and their photovoltaic performance.

The phases determined by XRD are supported by Raman scattering spectroscopy measurements of the films (Figure 4). The TiO<sub>2</sub>-1 thin film shows Raman peaks at 144, 399, 515, and 636 cm<sup>-1</sup> (Figure 4a), which indicate a pure anatase crystal phase based on a previous report.<sup>16</sup> The TiO<sub>2</sub>-3 thin film shows vibrational modes at about 244, 281, 409, 501, 589, and 633 cm<sup>-1</sup>, indicative of the brookite phase, and peaks at 230, 445, and 604 cm<sup>-1</sup>, indicative of a rutile phase.<sup>16,46</sup> The TiO<sub>2</sub>-2 films contain a mixture of peaks that can be attributed to anatase, brookite, and rutile phases as a result of nitric acid incorporation. The lowest-frequency mode shifts slightly for these films to 146 cm<sup>-1</sup>, as compared to 144 cm<sup>-1</sup> for the pure anatase (TiO<sub>2</sub>-1). This might be caused by changes in crystallographic composition due to nitrogen doping attributed to the vibrations of Ti-N-O introduced by nitric acid and HMT.<sup>15</sup> Raman spectrum of the TiO<sub>2</sub>-4 thin film shows that PEG suppresses the formation of the rutile and brookite phases, also consistent with XRD data. The intensity of the 146 cm<sup>-1</sup> peak for the TiO<sub>2</sub>-3 film is higher and sharper than that of undoped TiO<sub>2</sub>, indicating good crystallinity and size uniformity of the TiO<sub>2</sub>/N film.

**4.2. Morphological Properties.** The composition of the thin films was observed to be a mix of individual particles interconnected with high porosity. However, TiO<sub>2</sub>-3 and TiO<sub>2</sub>-4 films were far more porous than the TiO<sub>2</sub>-1 and TiO<sub>2</sub>-2 films. This suggests that HMT and PEG promote porosity, as was previously demonstrated in the case of PEG interacting with TiO<sub>2</sub> systems.<sup>47</sup> The morphology was noticeably more evident by AFM due to an atomically flatter surface produced with thin films on the order of 150 nm in thickness. The surface properties of the TiO<sub>2</sub>/N films are expected to be important in determining how well the CdSe QDs can link to and interact with the TiO<sub>2</sub> nanoparticles. AFM images of all TiO<sub>2</sub> films functionalized with CdSe QDs clearly show the presence of QDs, as evidenced by the apparent flattening of the films in the AFM images (e.g., Figure 5 for the TiO<sub>2</sub>-3-TGA-CdSe film).

**4.3. Optical Properties.** A comparison of the absorption spectra of all samples under study shows that films without HMT and PEG (TiO<sub>2</sub>-1 and TiO<sub>2</sub>-2) have absorption around 340 and 400 nm, respectively. However, TiO<sub>2</sub>-3 and TiO<sub>2</sub>-4 films with HMT or HMT plus PEG have a red shift of the absorption edge toward the visible region at 600 nm for samples annealed at 550 °C due to the electronic transition of N 2p<sub>π</sub> to Ti d<sub>xy</sub> (Figure 7c and d).<sup>27</sup> The red-shift absorption can be attributed to the doping of nitrogen into the crystal lattice of TiO<sub>2</sub> due to the addition of HMT in the sol-gel solutions. TiO<sub>2</sub>-3 and TiO<sub>2</sub>-4 films and calcined powders are also yellowish in color, attributed to the presence of nitrogen that results in the effective narrowing of the band gap.<sup>27</sup> All of the films sensitized with CdSe QDs exhibit strong absorption at 560 nm, which is the characteristic excitonic absorption band of CdSe QDs (Figure 7e).

As shown in Figure 8, CdSe QDs in solution exhibit strong and narrow band edge emission at 580 nm. While the PL spectrum of the TiO<sub>2</sub>-3-TGA-CdSe film shows a weak and blue-shifted PL band peaked at 575.5 nm. These results suggest interactions between TiO<sub>2</sub> nanoparticles and CdSe QDs and likely electron injection from CdSe to TiO<sub>2</sub>. The small blue shift of the PL peak could be due to slight oxidation of the film exposed to the atmosphere and thus a decrease in CdSe QD size during the sensitization process.<sup>48</sup> The electron-transfer process indicated by PL quenching is supported by photoelec-

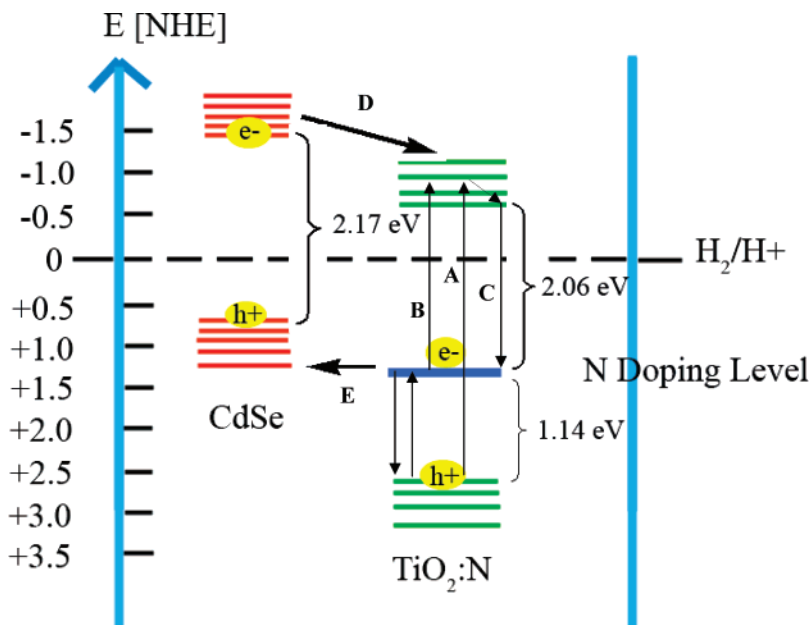


**Figure 12.** Schematic electronic band structure of 3.5 nm CdSe with an effective band gap of 2.17 eV and nanocrystalline TiO<sub>2</sub>/N with a 3.2 eV band gap, associated with normal TiO<sub>2</sub> and a N dopant state approximately 1.14 eV above the valence band, as reported by Asahi et al. (as denoted by the asterisk).<sup>27</sup> Different electron and hole creation, relaxation, and recombination pathways are illustrated, including (A) photoexcitation of an electron from the valence band (VB) to the conduction band (CB) of TiO<sub>2</sub>, (B) transition or photoexcitation of an electron from the N energy level to the CB of TiO<sub>2</sub>, (C) recombination of an electron in the CB of TiO<sub>2</sub> with a hole in the N energy level, (D) electron transfer or injection from the CB of a CdSe QD to the CB of TiO<sub>2</sub>, and (E) hole transfer from the VB of a CdSe QD to the N energy level. Note that not all of these processes can happen simultaneously, and many of these are competing processes.

trochemical measurements, to be discussed later. TiO<sub>2</sub>-1 and TiO<sub>2</sub>-2 films also have a PL emission at 580 nm due to CdSe QDs. However, there is no blue shift of the PL spectrum. This is possibly because the TiO<sub>2</sub>-1–CdSe and TiO<sub>2</sub>-2–CdSe have lower porosity than TiO<sub>2</sub>-3 and TiO<sub>2</sub>-4 and the CdSe QDs are not inside of the pores of the TiO<sub>2</sub> film and thereby have weak interactions with TiO<sub>2</sub> nanoparticles. This is illustrated schematically in Figure 1d. The average QD size is estimated to be 3.5 nm based on the absorption spectrum.<sup>49</sup>

**4.4. Photoelectrochemical and Photovoltaic Characterization.** As summarized in Table 1, thin and thick films sensitized with CdSe QDs show enhanced photocurrents and power conversion efficiency under white light, in comparison to films without sensitization of the CdSe QDs. The greatest enhancement was observed for TiO<sub>2</sub> films doped with nitrogen and simultaneously sensitized with CdSe QDs. What is interesting is that the QD-sensitized TiO<sub>2</sub>/N shows much larger enhancement than that of the simple sum of just N doping and only QD sensitization, especially in terms of photocurrents (Figure 9). One possible explanation is that N doping alters the surface property of the TiO<sub>2</sub> film so that the interaction between TiO<sub>2</sub> and CdSe QDs becomes stronger and allows for more efficient electron injection. XPS data also revealed a localization of nitrogen upon the surface (Figure 2b), and binding between exposed Cd<sup>2+</sup> and surface nitrogen atoms on TiO<sub>2</sub> could also increase interaction. The porosity of the TiO<sub>2</sub> film could also be effected by N doping that, in turn, influences how the CdSe QDs enter the pores and adsorb onto the TiO<sub>2</sub>/N nanocrystalline surface. The mixed brookite and rutile phases could also have some effect on the CdSe–TiO<sub>2</sub> interaction.

For the thick TiO<sub>2</sub>-1 and TiO<sub>2</sub>-2 films, it was also observed that a layer of CdSe QD film formed on the TiO<sub>2</sub> film surface. This seems to indicate that CdSe QDs did not all disperse into the pores of the TiO<sub>2</sub> films efficiently and were instead localized upon the TiO<sub>2</sub> surface. Therefore, CdSe QDs inject electrons mainly into the TiO<sub>2</sub> film surface, with CdSe QDs in contact

with a thin layer of TiO<sub>2</sub> nanoparticles, which could possibly explain why the short-circuit current, FF, and conversion efficiency are low for these two films. However, the conversion efficiency of TiO<sub>2</sub>-2 is higher than that of TiO<sub>2</sub>-1, probably due to nitrogen residues from the nitric acid added to the TiO<sub>2</sub> sol.

In comparison to the thick TiO<sub>2</sub>-3–TGA–CdSe film with the highest power conversion efficiency ( $\eta = 0.84\%$ ), the TiO<sub>2</sub>-4–TGA–CdSe (CdSe QD sensitized with HMT and PEG) has a lower conversion efficiency. This could possibly be due to a weakened interaction between CdSe QDs and TiO<sub>2</sub> nanoparticles caused by hydrocarbon species on the TiO<sub>2</sub> surface from uncombusted poly(ethylene glycol) (PEG). It is clear that IPCE is enhanced when the films are sensitized with CdSe QDs (Table 2) due to their strong visible absorption and electron injection. The highest IPCE percentage was found for TiO<sub>2</sub>-3–TGA–CdSe films (95% in 300 nm), where the larger content of brookite and rutile phases of the TiO<sub>2</sub>/N was present. The lower IPCE in TiO<sub>2</sub>-1 samples is possibly due to the lower porosity and probably due to the presence of the anatase crystalline phase (Figure 10). The performance of the solid solar cell is similar to that reported previously,<sup>50</sup> as shown in Figure 11. In this case, the highest IPCE is 6% at 400 nm and a strong response, larger than 4%, was observed at 600 nm. The first increase at 600 nm is attributed to the absorption onset of the 4.6 nm QDs utilized to sensitize the TiO<sub>2</sub>-3–TGA–CdSe film. The direct overlap with the first excitonic band (inset figure 11) of the CdSe QDs with the IPCE measurements confirms the electron injection into the TiO<sub>2</sub> conductive band. This, in turn, confirms the important role of the QDs to harvest photons and increase the generated photocurrent. All of these results indicate the sensitive dependence of the cell performance on the film porosity, QD–TiO<sub>2</sub> interaction, and N doping.

The electronic band structure of the CdSe QD and TiO<sub>2</sub>/N could help to better understand the reason behind the increased performance in TiO<sub>2</sub>/N thin films sensitized with CdSe. Figure 12 shows different electron–hole relaxation, recombination

pathways, and band structures of both CdSe QDs with a band gap of 2.17 eV (3.5 nm in average diameter) and nitrogen-doped TiO<sub>2</sub> with an overall band gap of 3.2 eV at pH = 7. The band diagrams of CdSe and TiO<sub>2</sub>/N have both been placed in relation to the normal hydrogen electrode (NHE). CdSe QDs of 3.5 nm have a top valence band position of ~+0.7 V and a conduction band of approximately -1.4 V based on previous reports.<sup>38</sup> The band structure of TiO<sub>2</sub>/N, in turn, has a valence band at ~+2.6 V and a conductive band at approximately -0.6 V based on the work by Sakthivel and Kisch.<sup>51,52</sup> N doping introduces a state at 1.14 eV above the valence band and 2.06 eV (600 nm absorption onset) below the conduction band of TiO<sub>2</sub>.<sup>28</sup> Several groups have also reported an absorption onset at 600 nm via reflectance spectroscopy.<sup>29,33,53</sup> Incorporation of nitrogen into nanocrystalline TiO<sub>2</sub> acts as an electron acceptor site within the TiO<sub>2</sub> band gap and effectively should be considered as a p-type doping. This state acts as an electron acceptor site within the TiO<sub>2</sub> band gap.<sup>27</sup> Now, it is still important to consider the typical n-type behavior of TiO<sub>2</sub> as a result of oxygen vacancies in the crystal lattice,<sup>54</sup> which therefore act as donor sites within the structure and effectively increase the Fermi level ( $E_F$ ) to more negative potentials (versus NHE).<sup>32,55</sup> The band gap dopant N state is populated, as evidenced by the weak absorption onset at 600 nm (2.06 eV) explained by Asahi et al. as a N 2p<sub>π</sub> to Ti d<sub>xy</sub> transition.<sup>27</sup> Due to the relatively weak absorption of this N 2p<sub>π</sub> to Ti d<sub>xy</sub> electronic transition in comparison to the quantum-confined CdSe transition (1S<sub>h</sub>1S<sub>e</sub>) transition, we expect that, for the CdSe QD-sensitized TiO<sub>2</sub>/N films, the optical absorption is dominated by the CdSe QDs.

To understand the charge-transfer and recombination kinetics, we will ignore the weak absorption due to N doping for the QD-sensitized TiO<sub>2</sub>/N film. In this case, photoexcitation of the CdSe QD generates a hole in its valence band and an electron in its conduction band. The electron in the conduction band of the CdSe QD is injected into the conduction band of TiO<sub>2</sub> (left to right black arrow (D)), and the transfer of the hole in the valence band of CdSe can be mediated by the electron-occupied N state (right to left black arrow (E)).<sup>56</sup> The energy level of the N state is close to the top of the valence band of CdSe, and this proximity in energy will aid in the hole (or electron)-transfer process. Since this only exists for the CdSe QD-sensitized and N-doped TiO<sub>2</sub> film, the N-mediated hole transport may be the key to the enhanced photoelectrical response of this film compared to that of TiO<sub>2</sub> films with only N doping or only QD sensitization. This is possible, especially considering that the hole transport is often the limiting step for overall charge transport in nanoparticle films.

It is clear that N doping into TiO<sub>2</sub> has introduced extra pathways for the charge carriers that could be beneficial for overall charge transport and thereby cell performance. Optimization of the system via an increased dopant level (currently 0.6–0.8%; see Table 1) and manipulation of the capping agents of CdSe may further enhance the photocurrent density as well as power conversion efficiency above that of 0.84%, which is currently observed.

## 5. Conclusions

Several TiO<sub>2</sub> films with nitrogen doping and/or CdSe QD sensitization have been systematically investigated using a combination of synthetic, spectroscopic, XRD, XPS, microscopy, and electrochemistry techniques. The structure of TiO<sub>2</sub>/N has been found to be generally a mixture of anatase, brookite, and rutile phases. Nitrogen doping into the TiO<sub>2</sub> lattice results

in a red shift of the electronic absorption and enhanced photocurrent response of relative to undoped TiO<sub>2</sub> films. In addition, CdSe QDs linked to TiO<sub>2</sub>/N nanoparticles were found to significantly increase the photocurrent and power conversion of the films compared to those of standard TiO<sub>2</sub>/N films without QD sensitization. The IPCE is 6% at 400 nm for TiO<sub>2</sub>/N-TGA-CdSe solid-state solar cells and 95% for TiO<sub>2</sub>/N-TGA-CdSe films near 300 nm in a Na<sub>2</sub>S electrolyte, which is much higher than that for undoped TiO<sub>2</sub> with QD sensitization or TiO<sub>2</sub>/N without QD sensitization. A power conversion efficiency ( $\eta$ ) of 0.84% was found along with a fill factor (FF%) of 27.7% for 1100 nm thick TiO<sub>2</sub>/N-TGA-CdSe thin films. The results show that the combination of nitrogen doping and QD sensitization of the TiO<sub>2</sub> thin films is an effective way to enhance the photoresponse, which is promising for photovoltaic (PV) and photoelectrochemical applications.

**Acknowledgment.** We are grateful for financial support by BES of the U.S. Department of Energy (J.Z.Z.), UC-MEXUS (J.Z.Z.), CONACyT (T.L.L.), and the National Science Foundation of China (No. 20628303 (J.Z.Z. and J.H.L.) and 20435010 (J.H.L.)). We thank Claudia Heide Swanson and Leo Seballos for helpful discussions. We would also like to thank Dr. Christain D. Grant for stimulating conversations concerning solar cells. The single-crystal X-ray diffraction data in this work were recorded on an instrument supported by the National Science Foundation, Major Research Instrumentation (MRI) Program under Grant No. CHE-0521569.

## References and Notes

- (1) LoPiccolo, P. *Solid State Technol.* **2007**, *50*, 2.
- (2) O' Regan, B.; Gratzel, M. *Nature* **1991**, *353*, 737.
- (3) Greenham, N. C.; Peng, X. G.; Alivisatos, A. P. *Phys. Rev. B* **1996**, *54*, 17628.
- (4) Belver, C.; Bellod, R.; Fuerte, A.; Fernandez-Garcia, M. *Appl. Catal., B* **2006**, *65*, 301.
- (5) Gregg, B. A. *J. Phys. Chem. B* **2003**, *107*, 4688.
- (6) Hagfeldt, A.; Gratzel, M. *Acc. Chem. Res.* **2000**, *33*, 269.
- (7) Kamat, P. V. *J. Phys. Chem. C* **2007**, *111*, 2834.
- (8) Lokhande, C. D.; Park, B. O.; Park, H. S.; Jung, K. D.; Joo, O. S. *Ultramicroscopy* **2005**, *105*, 267.
- (9) Smestad, G. P.; Spiekermann, S.; Kowalik, J.; Grant, C. D.; Schwartzberg, A. M.; Zhang, J.; Tolbert, L. M.; Moons, E. *Sol. Energy Mater. Sol. Cells* **2003**, *76*, 85.
- (10) Khaselev, O.; Turner, J. A. *Science* **1998**, *280*, 425.
- (11) Parsons, C. A.; Peterson, M. W.; Thacker, B. R.; Turner, J. R.; Nozik, A. J. *J. Phys. Chem.* **1990**, *94*, 3381.
- (12) Colon, G.; Maicu, M.; Hidalgo, M. C.; Navio, J. A. *Appl. Catal., B* **2006**, *67*, 41.
- (13) Kim, Y. G.; Walker, J.; Samuelson, L. A.; Kumar, J. *Nano Lett.* **2003**, *3*, 523.
- (14) Toyoda, T.; Tsuboya, I.; Shen, Q. *Mater. Sci. Eng., C* **2005**, *25*, 853.
- (15) Wang, J. W.; Zhu, W.; Zhang, Y. Q.; Liu, S. X. *J. Phys. Chem. C* **2007**, *111*, 1010.
- (16) Djaoued, Y.; Bruning, R.; Bersani, D.; Lottici, P. P.; Badilescu, S. *Mater. Lett.* **2004**, *58*, 2618.
- (17) Huang, D. G.; Liao, S. J.; Liu, J. M.; Dang, Z.; Petrik, L. J. *Photochem. Photobiol., A* **2006**, *184*, 282.
- (18) Huang, L. H.; Sun, Z. X.; Liu, Y. L. *J. Ceram. Soc. Jpn.* **2007**, *115*, 28.
- (19) Nishijima, K.; Naitoh, H.; Tsubota, T.; Ohno, T. *J. Ceram. Soc. Jpn.* **2007**, *115*, 310.
- (20) Moribe, S.; Ikoma, T.; Akiyama, K.; Zhang, Q. W.; Saito, F.; Tero-Kubota, S. *Chem. Phys. Lett.* **2007**, *436*, 373.
- (21) Sathish, M.; Viswanathan, B.; Viswanath, R. P.; Gopinath, C. S. *Chem. Mater.* **2005**, *17*, 6349.
- (22) Beranek, R.; Kisch, H. *Electrochem. Commun.* **2007**, *9*, 761.
- (23) Chen, H. Y.; Nambu, A.; Wen, W.; Graciani, J.; Zhong, Z.; Hanson, J. C.; Fujita, E.; Rodriguez, J. A. *J. Phys. Chem. C* **2007**, *111*, 1366.
- (24) Yin, S.; Ihara, K.; Aita, Y.; Komatsu, M.; Sato, T. *J. Photochem. Photobiol., A* **2006**, *179*, 105.
- (25) Wu, J. M.; Qi, B. *J. Phys. Chem. C* **2007**, *111*, 666.

- (26) Yin, S.; Komatsu, M.; Zhang, Q. W.; Saito, F.; Sato, T. *J. Mater. Sci.* **2007**, *42*, 2399.
- (27) Asahi, R.; Morikawa, T.; Ohwaki, T.; Aoki, K.; Taga, Y. *Science* **2001**, *293*, 269.
- (28) Di Valentin, C.; Pacchioni, G.; Selloni, A.; Livraghi, S.; Giamello, E. *J. Phys. Chem. B* **2005**, *109*, 11414.
- (29) Chen, X. B.; Burda, C. *J. Phys. Chem. B* **2004**, *108*, 15446.
- (30) Reyes-Garcia, E. A.; Sun, Y. P.; Reyes-Gil, K.; Raftery, D. *J. Phys. Chem. C* **2007**, *111*, 2738.
- (31) Wan, L.; Li, J. F.; Feng, J. Y.; Sun, W.; Mao, Z. Q. *Appl. Surf. Sci.* **2007**, *253*, 4764.
- (32) Livraghi, S.; Paganini, M. C.; Giamello, E.; Selloni, A.; Di Valentin, C.; Pacchioni, G. *J. Am. Chem. Soc.* **2006**, *128*, 15666.
- (33) Burda, C.; Lou, Y. B.; Chen, X. B.; Samia, A. C. S.; Stout, J.; Gole, J. L. *Nano Lett.* **2003**, *3*, 1049.
- (34) Leschkies, K. S.; Divakar, R.; Basu, J.; Enache-Pommer, E.; Boercker, J. E.; Carter, C. B.; Kortshagen, U. R.; Norris, D. J.; Aydil, E. S. *Nano Lett.* **2007**, *7*, 1793.
- (35) Levy-Clement, C.; Tena-Zaera, R.; Ryan, M. A.; Katty, A.; Hodes, G. *Adv. Mater.* **2005**, *17*, 1512.
- (36) Robel, I.; Kuno, M.; Kamat, P. V. *J. Am. Chem. Soc.* **2007**, *129*, 4136.
- (37) Somasundaram, S.; Chenthamarakshan, C. R.; de Tacconi, N. R.; Ming, Y.; Rajeshwar, K. *Chem. Mater.* **2004**, *16*, 3846.
- (38) Robel, I.; Subramanian, V.; Kuno, M.; Kamat, P. V. *J. Am. Chem. Soc.* **2006**, *128*, 2385.
- (39) Liu, H. Y.; Gao, L. *J. Am. Ceram. Soc.* **2005**, *88*, 1020.
- (40) Nguyen, V. N. H.; Amal, R.; Beydoun, D. *J. Photochem. Photobiol., A* **2006**, *179*, 57.
- (41) Niitsoo, O.; Sarkar, S. K.; Pejoux, C.; Ruhle, S.; Cahen, D.; Hodes, G. *J. Photochem. Photobiol., A* **2006**, *181*, 306.
- (42) Qu, L. H.; Peng, Z. A.; Peng, X. G. *Nano Lett.* **2001**, *1*, 333.
- (43) Mueller, N.; Tenne, R.; Cahen, D. *J. Electroanal. Chem.* **1981**, *130*, 373.
- (44) Ueno, Y.; Minoura, H.; Nishikawa, T.; Tsuiki, M. *J. Electrochem. Soc.* **1983**, *130*, 43.
- (45) Grant, C. D.; Schwartzberg, A. M.; Smestad, G. P.; Kowalik, J.; Tolbert, L. M.; Zhang, J. Z. *Synth. Met.* **2003**, *132*, 197.
- (46) Li, J. G.; Ishigaki, T.; Sun, X. D. *J. Phys. Chem. C* **2007**, *111*, 4969.
- (47) Liu, X. X.; Jin, Z. G.; Bu, S. J.; Yin, T. *J. Sol-Gel Sci. Technol.* **2005**, *36*, 103.
- (48) Gerischer, H.; Lubke, M. *J. Electroanal. Chem.* **1986**, *204*, 225.
- (49) Yu, W. W.; Qu, L. H.; Guo, W. Z.; Peng, X. G. *Chem. Mater.* **2003**, *15*, 2854.
- (50) Grant, C. D.; Schwartzberg, A. M.; Smestad, G. P.; Kowalik, J.; Tolbert, L. M.; Zhang, J. Z. *J. Electroanal. Chem.* **2002**, *522*, 40.
- (51) Sakthivel, S.; Janczarek, M.; Kisch, H. *J. Phys. Chem. B* **2004**, *108*, 19384.
- (52) Sakthivel, S.; Kisch, H. *ChemPhysChem* **2003**, *4*, 487.
- (53) Gole, J. L.; Stout, J. D.; Burda, C.; Lou, Y. B.; Chen, X. B. *J. Phys. Chem. B* **2004**, *108*, 1230.
- (54) Frank, S. N.; Bard, A. J. *J. Am. Chem. Soc.* **1975**, *97*, 7427.
- (55) Nowotny, J.; Bak, T.; Nowotny, M. K.; Sheppard, L. R. *J. Phys. Chem. B* **2006**, *110*, 18492.
- (56) Norris, D. J.; Bawendi, M. G. *Phys. Rev. B* **1996**, *53*, 16338.